Research Article Vol. 33, No. 2 / 27 Jan 2025 / Optics Express 1772
Optics EXPRESS

Point spread function measurements for underwater imaging: an analysis of wavelength-specific behavior for image deconvolution

JENDRIK SCHMIDT,[1,*] ENNO PETERS,[1] MAURICE STEPHAN,[1] AND OLIVER ZIELINSKI[2]

[1]German Aerospace Center (DLR e.V.), Institute for the Protection of Maritime Infrastructures, Fischkai 1, 27572 Bremerhaven, Germany
[2]Leibniz-Institut für Ostseeforschung Warnemünde (IOW), Seestraße 15, 18119 Rostock, Germany
*Jendrik.Schmidt@dlr.de

Abstract: Underwater optical imaging, especially in coastal waters, suffers from reduced spatial resolution and contrast by forward scattered light. With the increased number of hyper- and multi-spectral imaging applications, the effect of the point spread function (PSF) at different spectral bands becomes increasingly more relevant. In this work, extensive laboratory measurements of the PSF at 450, 500, 550, 600 and 650 nm in different turbidity have been carried out. Measurements were performed in deionized water with added scattering agent Maalox and in selected natural waters. The experimental setup and measurement routine, including a HDR camera calibration allowing PSF measurements at more than 6 orders of magnitude, is described in detail. Measured PSFs are compared and discussed in terms of wavelength-specific slope behavior, showing significant shape differences between color channels with increasing Maalox concentration. Image deconvolutions of a test target with correct and wrong color PSF indicate the relevance of wavelength-specific PSF consideration, especially in correcting channels of longer wavelengths. The results also indicate, that PSFs derived from models that are based on single wavelength PSF measurements can be used to effectively restore images at different wavelength when acquired over long scattering ranges and being scaled properly.

1. Introduction

Optical underwater imaging is strongly affected by high particle concentrations and therefore by multiple scattering, which is in particular relevant in coastal zones, harbours and other turbid areas. Image degradation caused by scattering affects a variety of applications of underwater optical systems ranging from inspections of offshore infrastructures, ships and unexploded ordnances to habitat monitoring, optical underwater communication and crime investigation. Blurring of the image is predominantly determined by the propagation of light through the water and in particular by scattering events. The point spread function (PSF) describes the sum of all scattering contributions to the image, which becomes increasingly important with increasing particle concentrations and light path lengths.

In the past, extensive effort was put into understanding and measuring PSFs in the ocean, coastal areas and harbours [1–3]. More recent research focused heavily on PSF and water property modeling through radiative transfer theory, while the foundation for widely used models was layed earlier by Well's small angle approximation [4] and Duntley's [5] and Dolin's [6] empirical studies, which were later summarized and compared by Hou [7]. PSFs have been mainly measured at a single wavelength around 532 nm, as green light typically shows the best

#541377 https://doi.org/10.1364/OE.541377
Journal © 2025 Received 5 Sep 2024; revised 19 Dec 2024; accepted 21 Dec 2024; published 13 Jan 2025

Optics EXPRESS

transmission in a large variety of waters [8,9]. However, especially in coastal zones like the German Bight, which are extensively used by economical and governmental stakeholders, the wavelength of best transmission often shifts towards the upper end of the visible spectrum [10], making these wavelengths interesting in imaging applications. In addition, with the increasing use of high resolution, focal plane array, multi- and hyperspectral optical systems in e.g. seabed and habitat monitoring, archaeology and sea-floor mapping [11,12], the image formation at different wavelengths becomes of greater interest.

Also, the PSF is especially critical in active imaging devices like range-gating systems [13,14], which are stronger affected by forward scattering, because of their enhanced imaging range in scattering waters. As the point spread function is equivalent to the beam spread function (widening of a collimated beam) [15], spectral PSF analysis is also of interested for multi-wavelength emitter design and directed light communication.

While there are multiple spectral dependency models for volume scattering functions and scattering coefficients [16,17] and thus the ability to model PSFs at different wavelengths, e.g. by Monte Carlo simulations, there is still a lack of experimental measurements of multi-spectral PSFs. A deeper understanding of PSF behaviour at a variety of wavelengths allows more precise estimations of their influence on multi-spectral imaging and encourages directed research and instrument development to improve image quality, especially in coastal and harbour waters. Therefore, in this work, the PSF is observed with regard to the attenuation lengths to the source, respectively beam attenuation coefficient, the particle size distribution (PSD) and the emitted wavelength (at 450, 500, 550, 600, 650 nm).

In addition, deconvolution is a well known image restoration technique, reducing blur and increasing image contrast [18,19]. As the correct assumption of the PSF plays a major role in this process, the influence of wavelength-specific PSF differences on restoration results is investigated.

This work is structured into six parts describing A) the applied camera high dynamic range (HDR) calibration to measure the PSF over several orders of magnitude with a non-scientific camera, B) the experimental setup, instrumentation and measurement methods, as well as C) water properties, followed by D) discussions of the resulting wavelength-specific PSFs and E) its influence on image formation and deconvolution. This is supplemented by F) a critical discussion of the transferability of performed laboratory measurement results to natural waters.

2. HDR camera calibration for PSF measurements

The PSF describes the apparent normalized radiance of an unresolved Lambertian point source and can be measured by tuning the angle θ between the optical axis of a photodetector with a sufficient narrow field of view (focused onto the spherical surface at emitter distance) with respect to the axis of maximum intensity of a Lambertian source [2] as shown in Fig. 1(a). When using a camera receiver focused onto the source, each pixel can be approximated as such a small angle detector seeing the apparent radiance in a defined angle θ from the optical axis of the Lambertian emitter allowing simultaneous measurements of multiple PSF angles (see Fig. 1(b).

Typically, PSF measurements [1,20] range over several orders of magnitude, which can not be covered by the used 12-bit camera within a single acquisition at a fixed exposure time. Additionally, the sensitivity of a non-scientific camera can not be assumed with certainty to be constant for different exposure time settings, because the true exposure times are influenced by limited rise and fall times and may therefore deviate from the set values (which is especially relevant at shorter exposure times). Also, keeping a constant f-number of the lens is important, as it is directly related to the spatial resolution of the camera system. Thus, in order to measure intensities over more than 6 orders of magnitude without changing the f-number, a high dynamic range calibration was performed. The calibration provides a set of conversion factors from incident photons to resulting image gray values, determined at multiple exposure times. Due to

Optics EXPRESS

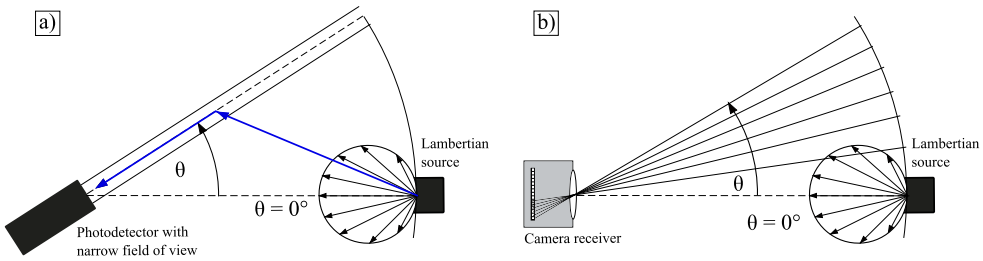

Fig. 1. a) PSF measurement using a single photodetector and rotating detector axis with respect to the emitter axis. b) PSF measurement using a camera focused into the distance of the source, measuring multiple angles simultaneously.

later normalization of the PSF, an absolute radiometric calibration is not required. The calibration as presented below also covers linearity error measurements at each exposure time, allowing to define the gray value limits in a single image to stay within a defined linearity error.

Therefore, as illustrated in Fig. 2, an integrating sphere of 50 mm diameter (Thorlabs IS200-4) was illuminated by a Halogen light source and the radiance L within the sphere was measured by a calibrated photodetector (Thorlabs S120C detector head with Thorlabs PM100 USB power meter) while exposing the lens-less camera at 11 different exposure times ranging from 1 µs to 100 ms. The sensor was placed in r_{cam} = 50 mm distance to the exit port of the integrating sphere with d_{port} = 12.5 mm, corresponding to an f-number of d_{port}/r_{cam} = 4 [21]. In this setup, spatial inhomogeneity from the center to the corners of the acquired images was below ±10%.

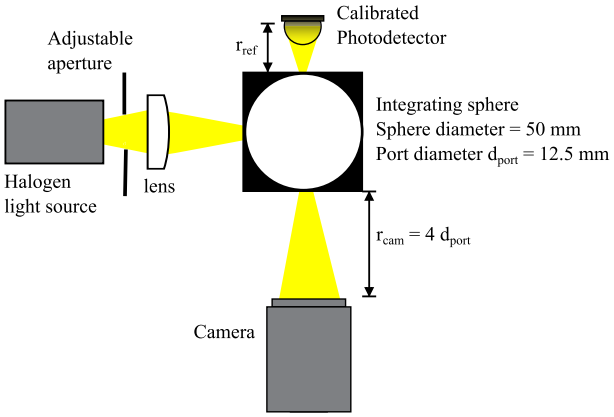

Fig. 2. Setup for camera HDR calibration: A halogen light source is focused into an integrating sphere. Radiance inside the integrating sphere is observed by a calibrated photodetector and can be controlled by an adjustable aperture in front of the light source.

At a selected exposure time, bright images were acquired at 12 different sphere radiances, set by an adjustable aperture in front of the light source in such a way, that the 12-bit pixel-depth of the camera was covered, i.e. 12 different grayscale images from dark to bright were acquired for each exposure time. In addition, a dark image with turned off light source was acquired for dark correction. In order to eliminate temporal noise, each image consisted of 100 individual images M, that were averaged. After dark correction by subtraction of the mean dark image M_{dark} from the mean bright image M_{bright}, the dark corrected mean gray value $\mu(t_{exp}, L)$ over all pixel rows i_{rows} and columns j_{cols} of the sensor was calculated for each exposure time t_{exp} and

Optics EXPRESS

sphere radiance L.

$$\mu(t_{exp}, L) = \frac{1}{i_{rows} \cdot j_{cols}} \sum_{i_{rows}} \sum_{j_{cols}} \left(\overline{M_{bright}(t_{exp}, L)} - \overline{M_{dark}(t_{exp}, L = 0)} \right) \tag{1}$$

As a result, the characteristic curve, which is the image gray value as a function of the sensor irradiance, was obtained. This curve was linear fitted to obtain the mean conversion parameters. This procedure was repeated for each of the 11 different exposure times resulting in 11 fitted characteristic curves. Due to the measurement of the sphere radiances with the high dynamic range of the photodetector these curves, and therefore their mean conversion parameters, can be set into relation with each other for all 11 selected exposure times. Figure 3 shows the HDR calibration result, i.e. the linear fits of the characteristic curves for different exposure times. Irradiance is normalized to irradiance L_0 at t_{exp} = 1 µs and μ = 3000 for better demonstration that the performed calibration allows PSF measurements over more than 6 orders of magnitude. Additionally, in the course of this calibration, the linearity error at each exposure time could be determined as the deviation of the measurement from the linear fit and was found to be better than 1.5% for used gray values between 50 and 3000.

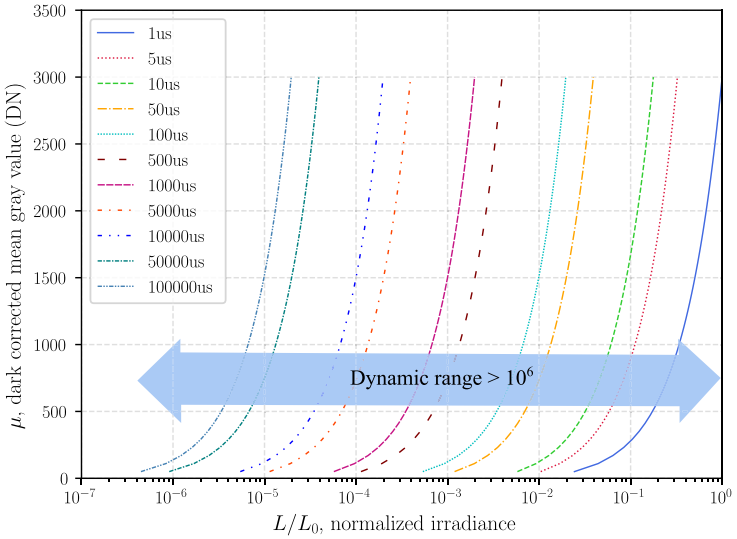

Fig. 3. HDR camera calibration: Color-coded are fitted dark corrected gray value curves for different exposure times.

3. Experiment description

3.1. Water tank

The PSFs have been measured with respect to the concentration of scatterers in the water and emission wavelength in a 1200 mm long, 500 mm wide and 500 mm high tank as sketched in Fig. 4. The walls and the floor of the tank have been covered by roughened black polymer sheets to prevent direct reflections. On the emitter side, light from a fiber-coupled, stabilized Xenon source (Thorlabs SLS205) with an approximately flat radiance spectrum in the visible range is filtered by 40 nm full width half maximum (FWHM) color filters at 450 nm, 500 nm, 550 nm, 600 nm and 650 nm center wavelengths. The spectrally filtered light exits the optical fiber through a 0.5 mm thick spectralon diffuser providing a nearly Lambertian source [22,23] with 4 mm diameter, which was mounted 165 mm above the floor of the tank and aligned to the optical axis

Optics EXPRESS

of the camera. Also, a pump was enabling constant circulation to prevent sedimentation of the added scattering agent and a hyperspectral transmissometer (TriOS Viper) with 250 mm optical path length was used to measure the beam attenuation coefficient throughout the experiment. On the receiver side, a Teledyne-e2v EV76C664 monochrome CMOS sensor with 1280 x 1024 pixels at 10 µm pixel pitch was combined with a low distortion double Gaussian 25 mm, F/4 lens, resulting in a spatial resolution of 0.0168° (0.29 mrad) per pixel in water, corresponding to a total diagonal angular field of view (aFOV) of 27.6°. Thus, 13.8° (240 mrad), which is half the aFOV, is the maximum measurable PSF angle. The spatial resolution of the setup is not diffraction limited as the diffraction limit Δl_{min} for resolving two point sources at a wavelength of λ = 650 nm and an f-number of f/# = 4 is well below the pixel pitch of the camera sensor used:

$$\Delta l_{min} = 1.22 \cdot \lambda \cdot f/\# \approx 3.2\ \mu\text{m} < 10\ \mu\text{m} \tag{2}$$

Additionally, the PSF of the lens was found to account for approx. 3% contrast loss between neighboring pixels.

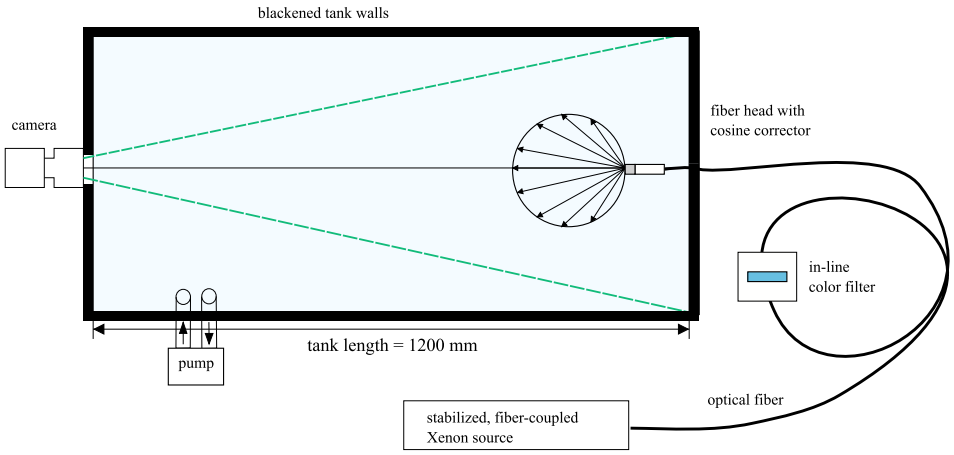

Fig. 4. Schematic PSF tank setup (top view): Light from a fiber-coupled Xenon source is spectrally filtered and emitted into the 1.2 m long tank through a cosine corrector. Tank walls are blackened and the point source is observed by a camera receiver. A homogeneous distribution of the scattering agent within the water is enabled by constant mixing by a pump, while a hyperspectral transmissometer was used to measure the beam attenuation coefficient.

3.2. PSF measurement routine

Measuring the PSF over the full range of the above described HDR calibration means acquisition of images at 11 different exposure times. To reduce temporal noise, 10 images were averaged for each exposure time. For each averaged image, a dark signal correction was applied and gray values over 3000 and below 50 were rejected in order to avoid consideration of saturated pixels and stay within the linearity error as determined above. By applying the HDR calibration factors, the gray values were then converted into normalized irradiances, yielding a single image for each PSF with up to 6 orders of magnitude pixel depth. As each pixel is representing a discrete angle θ between its viewing direction and the optical axis from camera to emitter, the radial symmetric PSF is simply obtained as irradiance from the center of the source. At this point, symmetry allows further averaging of the PSF, as up to 4 pixels represent the same angle θ if no angular binning is applied. After all, the irradiances were normalized to the source irradiance at $\theta = 0°$.

PSFs were measured in 11 different attenuation conditions, starting from deionized water and increasing the amount of scatterers and thus the beam attenuation coefficient in 10 steps. After

Optics EXPRESS

each addition of scatterers, the PSF was measured at 450, 500, 550, 600 and 650 nm in 1 m water path lengths between source and camera. Also note, that the whole experiment was conducted in a dark room in order to reduce the influence of ambient light sources.

4. Water properties

4.1. Measured beam attenuation coefficients

The water properties were varied through the addition of the magnesium hydroxide and aluminum hydroxide antacid Maalox (Maaloxan R Suspension), which was previously shown to be an appropriate scattering agent to simulate natural sea water [24–26] and is frequently used in scientific works [27,28]. Deionized water was required as basis, because Maalox flocculates in the presence of salts. According to Petzold's measurements [25], the Maalox particles contribute with ~ 92% to the scattering coefficient and only by the remaining ~ 8% to the absorption coefficient. Consequently, with increasing Maalox concentration in deionized water, the beam attenuation becomes dominated by scattering.

A detailed understanding of the Maalox solution properties is essential for the correct interpretation of the PSF measurements. Since the performed PSF measurements already included the measurement of the spectral beam attenuation coefficients $c(\lambda)$ at 11 different Maalox concentrations N_{Maalox}, the $c(\lambda)$ measurements were extended to 40 concentrations ranging from 0 mL/L to 0.17 mL/L. The increased number of measurements provides a more accurate determination of the wavelength-specific relation between $c(\lambda)$ and N_{Maalox}, contributing to this work and future experimental research including Maalox solutions.

Data measured with the transmissiometer with a spectral resolution of 2.2 nm was interpolated to fit the spectral resolution of Pope and Fry's pure water absorption measurements [29], which was used as pure water basis. Figure 5 shows how $c(\lambda)$ depends on the Maalox concentration. Towards higher Maalox concentrations, $c(\lambda)$ follows the trend of an exponential loss function rather than the pure water absorption curve. This monotone decrease is typical for non-algae particles like minerals [30], while for small concentrations, the measured absorption spectrum approaches the pure water spectrum from Pope and Fry.

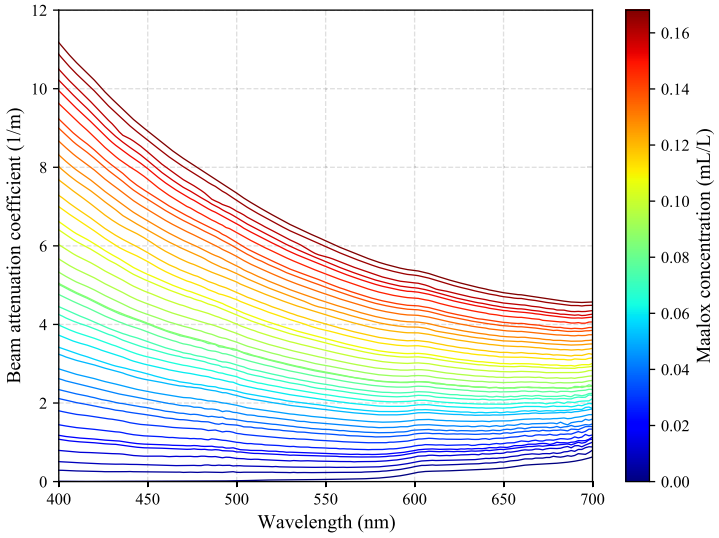

Fig. 5. Measured beam attenuation spectra at different Maalox concentrations. The lowest curve shows the Pope and Fry pure water absorption spectrum.

Optics EXPRESS

The red and blue markers in Fig. 6 exemplary show for c(λ = 450 nm) and c(λ = 650 nm), that the performed beam attenuation coefficient measurements follow a linear increase with Maalox concentration. In order to reduce the uncertainty of the beam attenuation coefficient for the PSF analysis, linear regressions (colored lines in Fig. 6) where applied for the relevant wavelengths of 450, 500, 550, 600 and 650 nm. Only the slope m of the linear curve was fitted, as the offset $c_0(\lambda)$ is given by the pure water absorption taken from [29].

$$c(\lambda) = m \cdot N_{Maalox} + c_0(\lambda) \tag{3}$$

Table 1 summarizes the fitted slopes m, $c_0(\lambda)$ and the resulting RMS errors for each of above mentioned wavelengths and additionally for the frequently in underwater imaging used wavelength of 532 nm. The following c(λ) in this work are derived from the Maalox concentration using Eq. (3) with linear regression results as listed in Table 1.

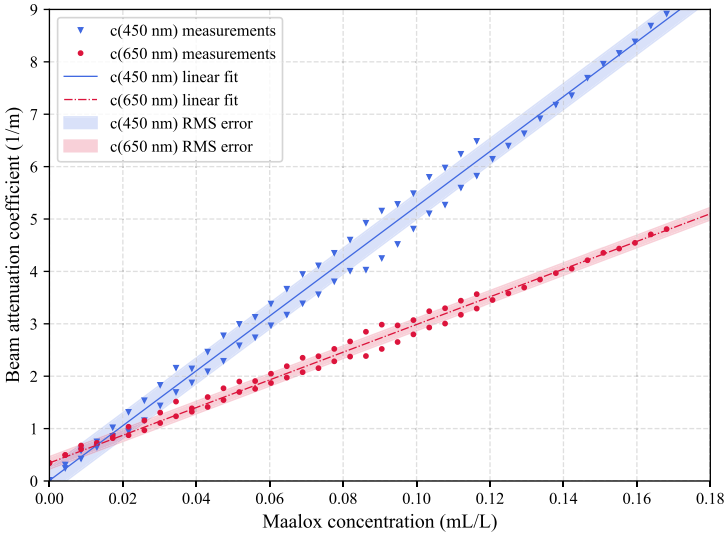

Fig. 6. Measurements and linear fits for c(λ = 450 nm) and c(λ = 650 nm) at different Maalox concentrations. The light colored areas indicate the RMS errors of the linear regression.

Table 1. Linear fit parameters for c-measurements over Maalox concentration at different wavelengths

λ (nm)	m (m^{-1} / (mL/L))	c_0[a] (m^{-1})	RMS error[b] (m^{-1})
450	52.34	0.009	0.244
500	43.19	0.020	0.199
532	37.94	0.044	0.175
550	35.62	0.056	0.163
600	30.33	0.220	0.141
650	26.42	0.344	0.117

[a]Pure water absorption as measured by Pope and Fry [29]
[b]Maalox concentration accuracy better than $4.5 \cdot 10^{-4}$ mL/L, dosed by pipette

Optics EXPRESS

4.2. Maalox scattering and extinction properties

As clearly seen from the beam attenuation coefficient measurements in Fig. 5, Maalox attenuates light at shorter wavelengths more than at longer wavelengths, predominantly because of scattering. Aiming to enrich the subsequent PSF analysis with a more detailed understanding of the scattering agent, a measurement of the particle size distribution (PSD) and a subsequent calculation of the extinction cross section according to Mie-Theory was performed. The PSD of the Maalox suspension was measured using a Horiba laser scattering particle size distribution analyzer LA-950. The measured number PSD in Fig. 7(a) shows a decreasing trend with particle diameter, which is typical for marine particle number distributions N'(D) and can be approximated by a power law (Junge) distribution [31,32]

$$N'(D) = k\left(\frac{D}{D_0}\right)^{-\gamma} \tag{4}$$

with particle diameter D and concentration k at a reference particle diameter D_0. A fit of Eq. (4) to the measured PSD obtained a PSD slope γ of 3.28, which is comparable to the typical slope ranges of 3.5 to 4 in natural marine waters [31].

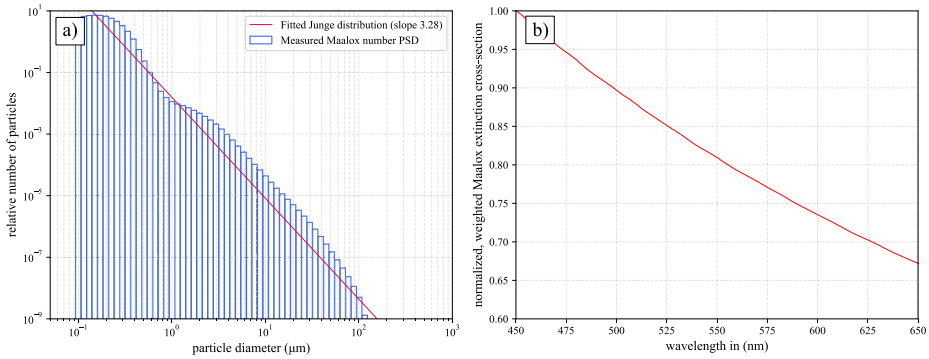

Fig. 7. a) Maalox number particle size distribution. b) Wavelength dependent mean extinction cross-sections in Maalox, derived from Mie-Theory and weighted with the number particle size distribution from a).

In order to approximate the wavelength-dependent attenuation and scattering behaviour, the mean extinction cross section according to Mie-Theory was calculated using Miepython [33], [34]. The refractive index of Maalox was approximated to be $n = 1.57$, based on the refractive indices of the main ingredients Aluminium Hydroxide (1.57) [35] and Magnesium Hydroxide (1.559, 1.580) [36]. Weighting the resulting extinction cross sections with the measured number PSD is a measure for the extinction probability of light at a specific wavelength in a unit volume of Maalox and is plotted in Fig. 7(b) after normalization to its extinction cross section at 450 nm. The resulting curve implies that the probability for a photon to be scattered or absorbed in Maalox is monotonously decreasing from 450 nm to 650 nm, which is in agreement with the measured beam attenuation spectra at higher Maalox concentration. Also, from Petzold [25] it is known, that the majority of the extinction cross section contributes to the scattering coefficient, which makes ~ 92% of the beam attenuation coefficient. Consequently, the extinction cross section gives a close approximation to the scattering cross section.

5. PSF results and discussion

The basis for the following wavelength-dependent analysis is an accurate measurement of the PSF as obtained from the measurement routine described in Section 3.2. In order to validate the

Optics EXPRESS

performed measurements, a comparison with the widely used model by Duntley [5] was done, showing good agreement, especially at larger angles. The blue markers in Fig. 8 show the PSF measured at λ = 550 nm and c = 1.6 m^{-1}, while the green line indicates the corresponding model by Duntley. At small angles, the model deviates from the measurement, because the blurred finite size source is imaged. With a source diameter of 4 mm, the unbiased, measured PSF begins at angles $\theta \approx>$ 2.5 mrad for the water path of r = 1 m.

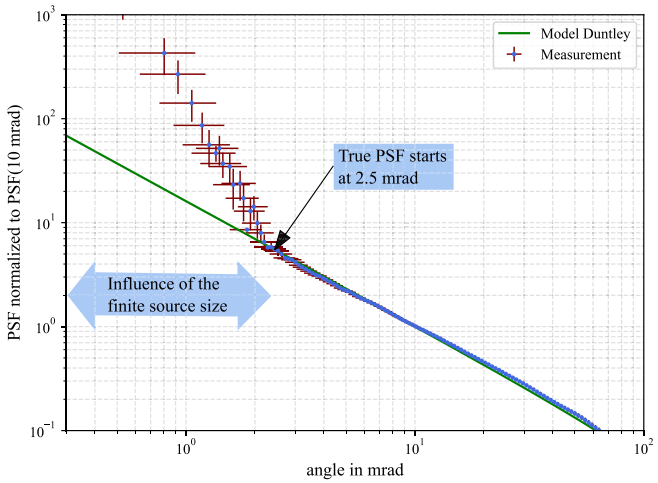

Fig. 8. Measured and modeled PSF (Duntley [5]) in a Maalox concentration of 43 µL/L at a wavelength of 550 nm, beam attenuation coefficient of 1.6 m^{-1} with r = 1 m water path and an absorption to attenuation coefficient ratio of 0.11. For reasons of better visibility, data was binned logarithmically between angles of 0 and 100 mrad

The main source of errors (see red bars in Fig. 8) in the PSF measurement at small angles is due to the spatial discretization by finite pixel size, which directly affects irradiance errors by preventing the exact determination of the source center (the optical fiber exit with mounted lambertian diffusor). However, with increasing angle this becomes less relevant. With decreasing values of the PSF, i.e. at larger angles, the irradiance accuracy of the camera measurements decreases because the signal to noise ratio decreases at low light levels.

All measured PSFs of a specific color are significantly flatter, respectively wider, in high Maalox concentrations (color coded, dashed lines in Fig. 9(a)) than in clearer water (color coded, solid lines in Fig. 9(a)). This holds true over the whole visible spectrum and is a direct result from the scattering probability increasing proportional to the number of Maalox particles within the optical path. In very clear water, the probability for light to be scattered is low, thus the PSF peaks towards θ = 0 mrad (dirac pulse), while at increasing Maalox concentrations, respectively attenuation lengths ($\tau = c \cdot r$), the PSF begins to flatten.

When analysing the color spread, i.e. the difference in slopes between PSFs of different wavelengths in Fig. 9(a), it is obvious, that in clear conditions, the color spread is significantly smaller than in the highly scattering medium. However, a more detailed analysis requires a quantitative determination of the PSF slope. As it can be seen from Fig. 8 and 9(a), the PSF outside the influence of the blurred source is almost linear in the double logarithmic plot within the considered angular measurement range. This is in agreement with former measurements by Voss and Frew [20,37], who derived an empirical model and proved it to be valid for their measurements within the 4 to 100 mrad range. Their model is defined as a linear function in the log-log range

$$PSF\,(\theta) = B \cdot \theta^{-m} \tag{5}$$

Optics EXPRESS

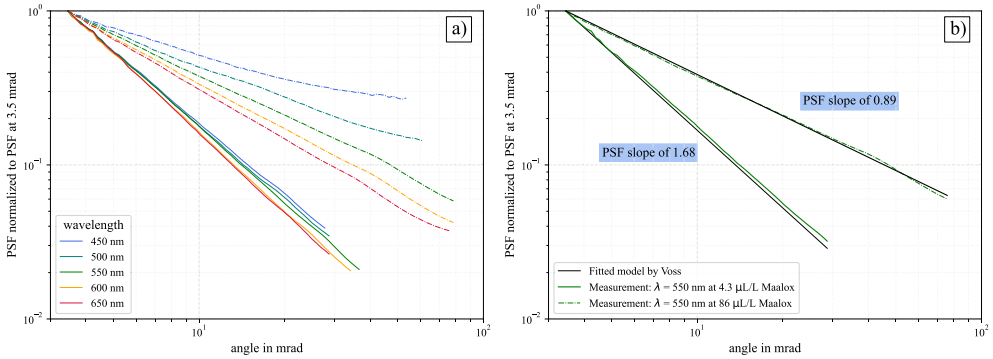

Fig. 9. a) PSF measurements at different wavelengths (color coded) in 4.3 µL/L (solid lines) and 86 µL/L (dashed lines) Maalox concentration, i.e. scattering conditions. b) Empirical model by Voss fitted to the λ = 550 nm measurements shown in Fig. 9(a).

with the constant B and the slope m. Model parameters B and m were fitted to our measurements, starting at angles of 2.5 mrad (making sure not to fit the blurred finite size source) and stopping at up to 100 mrad, depending on the measurable angular limit. The applied model fits our measurements very well, which can been seen from Fig. 9(b) showing the fits applied to the λ = 550 nm measurements from Fig. 9(a). At larger angles and especially at very high attenuation lengths, the measurements in Maalox begin to deviate from the linear model, which can be likely explained by the increased contribution of multiple scattering events and different optical constituents of the Maalox solution compared to the measurements in coastal, oceanic and harbour waters by Voss. However, with coefficients of determination of $R^2 \geqslant 0.98$ for all Maalox concentrations except the highest ones at 450 nm (R^2 = 0.83) and 500 nm (R^2 = 0.96), fitting Voss and Frew's model to our measurements seems a suitable choice, allowing a more quantitative analysis of PSF slopes.

Figure 10(a) shows the derived PSF slopes (colored markers) as a function of the scattering coefficient b(λ) in different Maalox solutions. The scattering coefficients are derived from c(λ) by subtraction of the pure water absorption and consideration of the Maalox a to c ratio introduced in Section 4.2. The PSF slopes m(λ) monotonously decrease with increasing b(λ) as a consequence of the raising scattering probability. Over the observed b(λ) range, a trend of longer wavelengths resulting in steeper PSF slopes is seen. However, this trend accounts only for a PSF slope variation of approximately 10% between wavelengths of 450 nm and 650 nm at a given scattering coefficient, which is minor compared to the overall PSF slope decrease with b(λ). This is in accordance with previous observations of single scattering phase functions in very clear and turbid waters, showing the scattering direction of a single scattering event in turbid waters to be a) generally more forward peaked and b) less wavelength-dependent [38]. However, when approaching the multiple-scattering regime, this single scattering effect gets dominated by the scattering probability, which itself is a function of wavelength. In other words: blue light might not scatter significantly broader in Maalox solutions than red light, but it gets scattered more often, leading to an overall wider PSF.

This becomes obvious in Fig. 10(b), showing the wavelength-specific PSF slopes to spread significantly with increasing Maalox concentration. From the corresponding PSF slope values listed in Table 2, it can be derived, that in clear water (0 µL/L Maalox), the PSF at λ = 650 nm is by a factor of 1.1 steeper than at λ = 450 nm. This increases up to a factor of 3.3 at the highest Maalox concentration of 107.8 µL/L Maalox and can be explained by the scattering probability decreasing with wavelength as a consequence of the spectral extinction cross section of the Maalox PSD, derived from Mie-Theory in Section 4.2, Fig. 7(b).

Optics EXPRESS

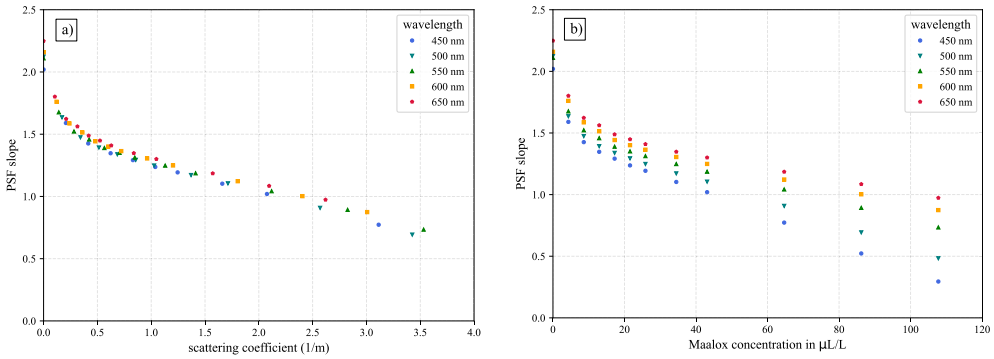

Fig. 10. PSF slopes measured at different wavelengths (color coded) over 1 m distance in Maalox solutions plotted a) in dependence of the scattering coefficient and b) depending on the Maalox concentration.

Table 2. Wavelength-specific, measured PSF slopes m(λ) for different Maalox concentrations N_{Maalox}.

N_{Maalox} (mL/L)[a]	m(450 nm)	m(500 nm)	m(550 nm)	m(600 nm)	m(650 nm)
0.0000	2.02	2.12	2.11	2.16	2.25
0.0043	1.59	1.64	1.68	1.76	1.80
0.0086	1.43	1.47	1.52	1.59	1.62
0.0129	1.35	1.39	1.46	1.51	1.56
0.0172	1.29	1.34	1.39	1.44	1.49
0.0216	1.24	1.29	1.35	1.40	1.45
0.0259	1.19	1.25	1.31	1.36	1.41
0.0345	1.10	1.17	1.25	1.31	1.35
0.0431	1.02	1.10	1.19	1.25	1.30
0.0647	0.77	0.91	1.04	1.12	1.19
0.0862	0.52	0.69	0.89	1.00	1.08
0.1078	0.29	0.48	0.73	0.87	0.97

[a]For conversion into beam attenuation coefficients see Eq. (3) and regression parameters in Table 1.

Overall these measurements indicate towards a significant wavelength influence on image formation, if there are strong variations in the scattering spectrum. Furthermore, it arises the question, whether or not an additional consideration of the PSF variation with wavelength is necessary, if a proper scaling with b(λ) was done.

6. Influence on image formation and deconvolution

As motivated in Section 1, the main purpose for PSF measurements performed here is the evaluation of its color-specific influence on image formation and deconvolution of blurred images. This is investigated in a second experiment in which images of an actual scene in Maalox solutions were acquired.

According to the fundamental principle of image formation, the acquired, blurred image g(x', y', z) can be described as the ideal, undisturbed image f(x, y, 0) convoluted with the PSF, where x and y denote a point (pixel) in the image observed over distance z [39,40]:

$$g(x', y', z) = f(x, y, 0) * PSF(x', y', z) \tag{6}$$

Optics EXPRESS

The PSF measurements described in the previous sections showed a smaller slope for shorter wavelengths, indicating that blue channels are blurred stronger than red channels at all Maalox concentrations. Figure 11 shows a comparison of color-filtered images of a test chart with black-white patterns of different spatial frequencies in 1 m distance. A severe contrast loss towards images acquired at shorter wavelengths can be seen, which is in agreement with the PSF at λ = 650 nm being 2.1 times steeper then at λ = 450 nm in the given Maalox concentration of 86.2 µL/L (refer to Table 2 or Fig. 10(b) above).

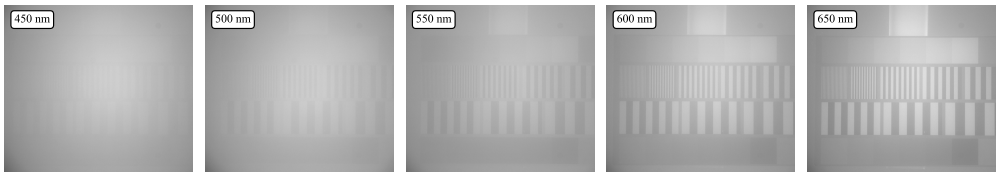

Fig. 11. Images acquired at different wavelengths using the same bandpass filters as in the PSF measurements. Acquired in 1 m distance at 86.2 µL/L Maalox concentration (c(550 nm) = 3.23 m^{-1}). Images are normalized to their mean gray value, for better contrast comparison by eye.

As image formation follows Eq. (6), with known PSF the ideal image can be recovered by deconvolution. However, since direct deconvolution through simple division in the frequency domain results in excessive noise amplification, more sophisticated algorithms are required. The Richardson-Lucy (RL) deconvolution [18,19] is a well tested approach in deblurring noisy images by solving a maximum likelyhood problem and is used in the following analysis.

To estimate the consequences of wavelength-specific PSF slopes for image restoration, the test chart as shown in Fig. 11 was used for the two examples of 450 nm and 600 nm, using the same camera and filter setup as in the PSF experiments. To ensure a matching with the PSF measurements, the target was placed in 1 m distance and the images were recorded at similar Maalox concentrations. In order to show the effects on image deconvolution with the correct color and the wrong color (too long wavelength) PSF, a raw image acquired at 450 nm was deconvolved (20 iterations) once with PSF(450 nm) and once with PSF(600 nm). This was repeated for an image acquired at 600 nm, allowing to additionally evaluate the influence of PSFs corresponding to too short wavelengths.

Figure 12(a)-(f) provides an overview of the resulting raw and deconvolved images for a rather low Maalox concentration of 21.6 µL/L, representing conditions with low color-dependence of the PSF slope. On the other hand, Fig. 12(g)-l shows the results at a higher Maalox concentration of 86.2 µL/L, representing conditions of a large PSF color spread. For better visualisation, a zoom into the spatial frequency pattern of interest is shown. At both Maalox concentrations, an increase of contrast after deconvolution with the correct PSF can be observed. However, hardly any difference is found for the 450 nm image between using the PSF at 450 nm or 600 nm for deconvolution (compare images in the first or third row). In contrast, deblurring a 600 nm image with a 450 nm PSF induces severe artifacts in the high Maalox concentration with its large PSF slope difference (see Fig. 12(k)). This can be explained by proneness of the RL-algorithm to PSF overestimation (too wide), leading to overcorrection.

For a more quantitative analysis, the line contrast along the green line in Fig. 12(a) was calculated for each raw image and combination of deconvolved images in Fig. 12. The contrast is defined as $(I_{max} - I_{min})/(I_{max} + I_{min})$, with I_{max}, I_{min} being the maximum, respectively minimum intensity (gray value) in a pattern of given spatial resolution. The reference contrast of the grey pattern in deionised water is approximately 66% and was measured at all 5 selected colors.

The high Maalox concentration scenario is especially of interest, as this is the scenario with the large color spread of the PSF slope and the large b(λ) difference, indicating a significant impact

Optics EXPRESS

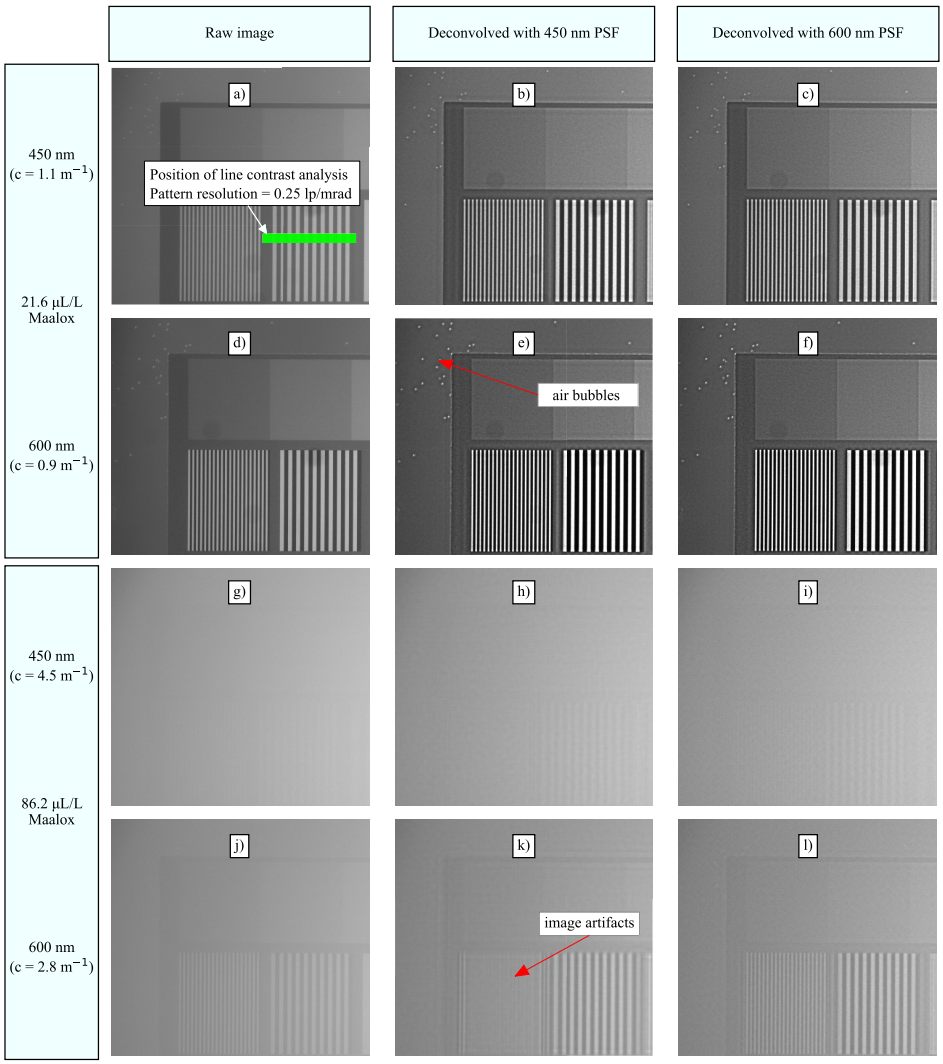

Fig. 12. Deconvolutions of a a test chart consisting of patterns of different spatial frequencies imaged at 450 nm and 600 nm over 1 m distance in two different Maalox concentrations (21.6 µL/L and 86.2 µL/L) using an iterative Richardson-Lucy approach. Raw images are deconvolved with correct and false color PSFs.

of correct or false color PSF selection for deconvolution. The yellow lines in the line analysis results in Fig. 13(a) and (b), show, that the line contrast of the image before deconvolution reduces in a high Maalox concentration of 86.2 µL/L, down to 6% at λ = 450 nm and 35% at λ = 600 nm. The deconvolution of the 450 nm image with either the correct color or false color PSF yields approximately the same contrast improvement (compare lightblue and brown lines in Fig. 13(a)), despite the red PSF being significantly steeper than the blue one. On the other hand, correct color deconvolution of the 600 nm image results in better contrast improvement compared to deconvolution with the wrong 450 nm PSF (improvement by a factor of 4.5 compared to 3.5). Additionally, when deconvolving with the shorter wavelength PSF, the line analysis confirms the induced image artifacts like overshoots seen in Fig. 12(k). Overall, the line analysis confirms the above described visual impression of deconvolution results.

Optics EXPRESS

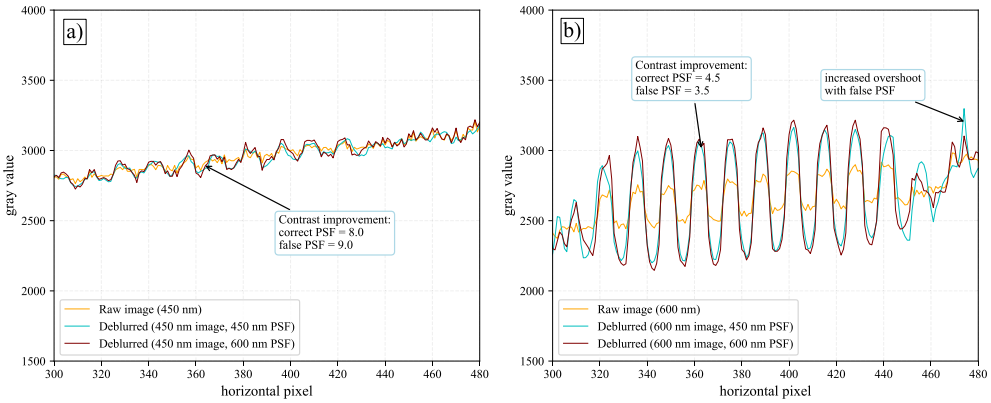

Fig. 13. Line contrast comparison for the 0.25 lp/mrad pattern at the position indicated Fig. 12(a) derived from a) 450 nm and b) 600 nm image, in high (86.2 µL/L) Maalox concentration before and after deblurring using 20 iterations of RL-deconvolution with correct and false color PSF. The reference contrast in deionised water between bright and dark stripes is approx. 66%.

The findings from the visual impression as well as the quantitative line contrast analysis of the deconvolution experiment lead to two conclusions:

- In lower Maalox concentrations corresponding to a rather flat beam attenuation and scattering spectrum with a small color-dependence of the PSF slope, a wavelength-specific PSF selection for image deconvolution has a minor influence on resulting image contrast improvements.
- In higher Maalox concentration with a large b(λ) and PSF color spread, care has to be taken especially when restoring long wavelength images through deconvolution. Assuming a shorter wavelength PSF (e.g. deconvolution of a 600 nm image with a 450 nm PSF) causes a loss in contrast improvement and likely induces severe image artifacts.

However, the findings from Section 5 showed the PSF to be dependent 1) of wavelength-specific scattering angle and 2) of wavelength-specific scattering probability b(λ). Since the deconvolution analysis above, does not distinguish between these two effects, another deconvolution analysis was performed, trying to separate them. Therefore we deconvolved an image acquired at 450 nm and a selected b with 1) its correct PSF and with 2) a 600 nm PSF corresponding to the same b. The latter is a PSF that is scaled to the correct scattering probability, but a false wavelength scattering angle. This represents the case of a PSF derived from a model based on a single wavelength (600 nm in this example) being used for restoration of an image acquired at a different wavelength. The comparison was done twice, once for a small b = 0.6 m^{-1} (single scattering) case and once for a large b = 3.1 m^{-1} (multiple scattering) case. Figure 14(a) and (c) show the corresponding 450 nm raw images. The line contrast of the 0.25 lp/mrad pattern improves with both PSFs after deconvolution (see Fig. 14(b) and (d)). However, in the b = 0.6 m^{-1} case, contrast improvement is less, if the false PSF is used (compare red dashed and yellow line in Fig. 14(b)), indicating the necessity to consider the wavelength-dependent scattering angle. On the other side in the b = 3.1 m^{-1} case seen in Fig. 14(d), this hardly affects the deconvolution results. Comparable results were seen, when correcting a 600 nm image at a selected b with its correct PSF and a 450 nm PSF at the same b.

The deconvolution analysis above shows, that the wavelength dependency of the PSF affects deblurring results in Maalox solutions in different ways:

Optics EXPRESS

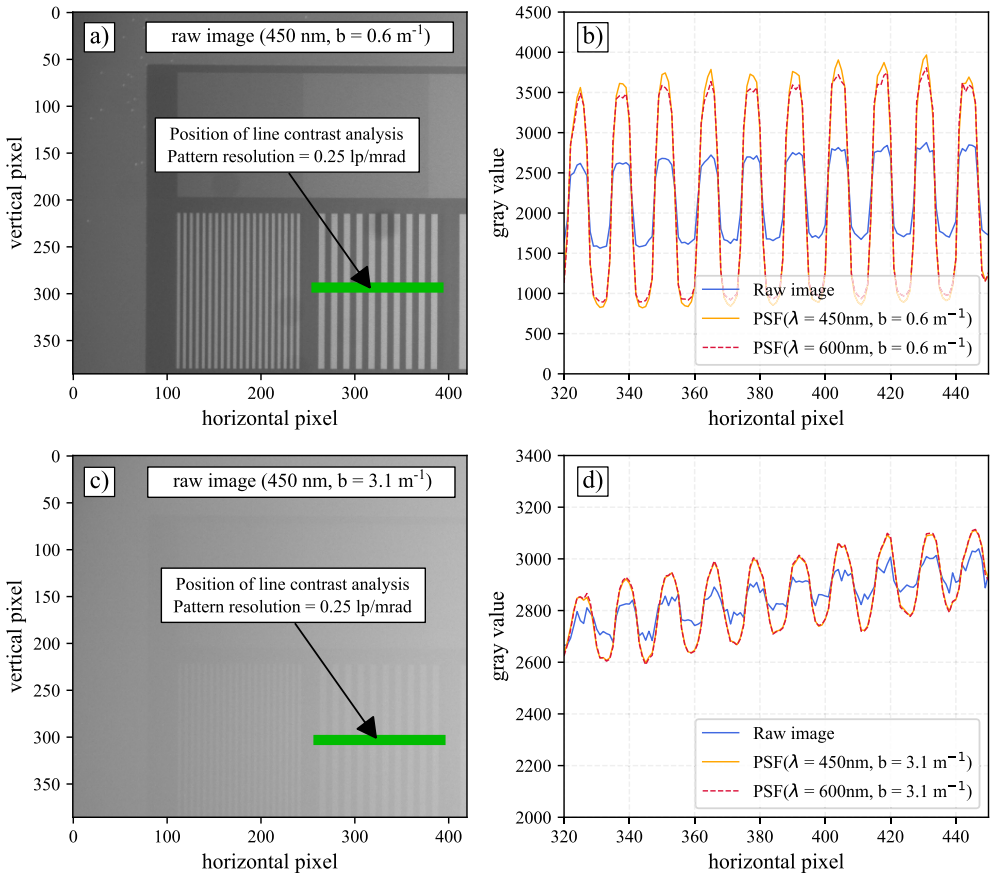

Fig. 14. Line contrasts b) and d) along the 0.25 lp/mrad pattern imaged at 450 nm over 1 m distance before and after deconvolution with different PSFs. The raw images acquired at a) b = 0.6 m^{-1} and c) b = 3.1 m^{-1} are deconvolved with correct and false color PSF at common scattering coefficients.

- In multiple scattering cases a false wavelength PSF selection can especially affect the deblurring of longer wavelength channels by inducing image artifacts. Furthermore in this case the need for a wavelength-specific PSF is mainly driven by the wavelength dependency of b(λ). The wavelength dependency of the scattering angle hardly contributes to the PSF differences with wavelength and is largely dominated by the differences in the b(λ) spectrum.
- Approaching more clear single scattering cases, a false wavelength PSF selection also can affect the deconvolution results. However, in this case the wavelength dependency of the scattering angle gains importance.
- In between there can be cases, especially with high overall scattering probability and a flat b spectrum (e.g. at 21.6 µL/L Maalox), where the wavelength dependency of the PSF has hardly any influence on image deconvolution.

7. Transferability of results to natural waters

Even though the measured PSFs show the typical curvature measured in previous works in the field and laboratory, and the empirical model by Voss [37] fits our measurements very well, care

Optics EXPRESS

has to be taken when transferring results from measurements made with Maalox to natural waters. Aiming to assess the transferability, additional PSF measurements in selected natural waters were performed. Following the experimental setup and analysis method described in Sections 3 and 5, the PSFs of water from the Weser river delta, a harbour basin and a freshwater lake near Bremerhaven, Germany were measured and wavelength-specific PSF slopes were derived. It has to be noted, that these measurements were taken after severe sedimentation occured, as initial beam attenuations ($c > 20\ m^{-1}$ for Weser river) were too strong to be measured with the given setup. The PSFs for the Weser river water were measured after 5 days of sedimentation (Weser river A) and after 10 days of sedimentation (Weser river B). However, it exemplarily illustrates the issues of transferring Maalox measurements to field applications.

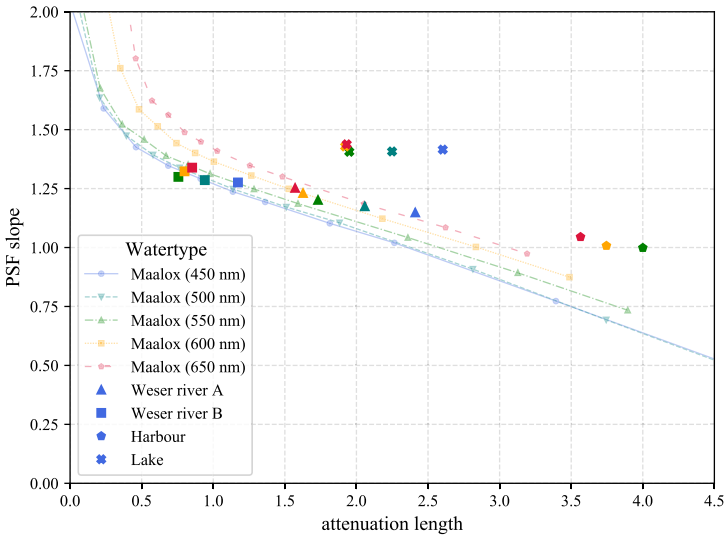

Fig. 15. PSF slopes measured in Maalox and different natural waters depending on the attenuation length.

Figure 15 shows the measured PSF slopes as a function of the attenuation length for these natural waters (indicated as markers in wavelength-corresponding colors) together with the Maalox solution measurements (indicated as light colored lines). PSF slopes of natural waters show obvious deviations from measurements in deionized water mixed with Maalox. In general, slopes observed at specific attenuation lengths tend to be steeper in natural waters than in Maalox solutions, which can be explained with absorption by Colored Dissolved Organic Material (CDOM), Phytoplankton (primarily Chlorophyll absorption), non-algae particles (NAP) and other non-organic, absorbing particles [41] adding to overall attenuation without widening the PSF. Also, the particles in the Weser river and harbour volume PSD were found to be significantly larger than in Maalox, which indicates for a different wavelength dependent scattering cross section, as well as changes in single scattering phase functions.

As Voss [37] and others discussed in previous work, changes in absorption to extinction ratio affect the PSF slope, which was not covered in our experiments, as all measurements were performed over 1 m distance and the small tank did not allow significant absorption to attenuation ratio changes due to limited optical path lengths. Also, it has to be considered that Maalox is a nearly perfect, quasi non-absorbing scatterer. Especially, the deviations of PSF in natural waters from Maalox, require follow-up studies using in-situ measurements and simultaneous absorption measurements.

Optics EXPRESS

8. Summary

The analysis of PSF shapes and slopes at wavelengths of 450, 500, 550, 600 and 650 nm in deionized water and various Maalox solutions at up to 5.6 attenuation lengths showed significant influences of the wavelength on PSF steepness. The performed PSF measurements show how the single scattering phase function and the scattering coefficient (scattering probability), which are both wavelength dependent, affect the PSF formation. The difference of the PSF slopes of two different colors where found to significantly increase with Maalox concentration, leading to PSF(λ = 650 nm) becoming up tof 3.3 times steeper than PSF(λ = 450 nm), which was found to be mainly caused by differences in the scattering coefficient with wavelength and not the shift of scattering angles. An analysis of deconvolutions of stripe patterns with correct and false wavelength PSFs in a second experiment showed, that careful scaling of the PSF with b(λ) is important, especially when imaging in the multi scattering regime and correcting longer wavelength channels. Exemplary deconvolutions showed that deblurring of images acquired at longer wavelengths suffers from induced artifacts if they are restored with shorter wavelength PSFs. Furthermore, the performed deconvolutions indicate, that the consideration of the wavelength dependency of the scattering angle is hardly relevant at large scattering lengths, but becomes more important approaching clear water and the single scattering regime. This indicates, that established PSF models based on single wavelength measurements may be used to model PSFs for deconvolution of images acquired in particle rich waters at different wavelengths, as long as they are modeled with b(λ) at the correct wavelength. However, results presented are concluded from experiments in Maalox solution and care has to be taken, when transferring results to natural waters.

Additionally, a camera HDR calibration method and measurement routine, enabling PSF measurements over up to 6 orders of magnitude, has been proposed and validated against the well known empirical model by Duntley [5], providing means for robust PSF measurements with simple hardware after careful instrument characterization.

The findings of this study support underwater optical research and development in laboratories using Maalox as main scattering agent, i.e. works on wireless optical communication [42] and underwater LiDAR [43] in terms of understanding how light propagates through multiple scattering processes. Furthermore, it provides an experimental basis for PSF contributions to multi- and hyperspectral underwater system design and applications, which is a growing research field.

Funding. Deutsches Zentrum für Luft- und Raumfahrt; Bundesministerium für Wirtschaft und Klimaschutz.

Acknowledgments. Financial support for the scientific work presented here was partly provided by Deutsches Zentrum für Luft- und Raumfahrt and by Bundesministerium für Wirtschaft und Klimaschutz (funding code 03SX551B) in the context of the REMAP project. The responsibility for the content of this publication lies within the author. We thank Elke Ahrensfeld from ICBM Wilhelmshaven, Germany for granting access to and supporting the particle size distribution measurements.

Disclosures. The authors declare that there are no conflicts of interest related to this article.

Data availability. Data underlying the results presented in this paper are not publicly available at this time but may be obtained from the authors upon reasonable request.

References

1. K. J. Voss and A. L. Chapin, "Measurement of the point spread function in the ocean," Appl. Opt. **29**(25), 3638–3642 (1990).
2. L. E. Mertens and F. S. Replogle, "Use of point spread and beam spread functions for analysis of imaging systems in water," J. Opt. Soc. Am. **67**(8), 1105–1117 (1977).
3. J. W. McLean and K. J. Voss, "Point spread function in ocean water: comparison between theory and experiment," Appl. Opt. **30**(15), 2027–2030 (1991).
4. W. H. Wells, "Loss of resolution in water as a result of multiple small-angle scattering," J. Opt. Soc. Am. **59**(6), 686–691 (1969).
5. S. Q. Duntley, "Light in the sea," J. Opt. Soc. Am. **53**(2), 214–233 (1963).

Optics EXPRESS

6. L. Dolin, G. Gilbert, I. Levin, *et al.*, "Theory of imaging through wavy sea surface," Inst. Appl. Phys. (RAS) (2006).
7. W. Hou, D. J. Gray, A. D. Weidemann, *et al.*, "Comparison and validation of point spread models for imaging in natural waters," Opt. Express **16**(13), 9958–9965 (2008).
8. N. G. Jerlov, *Optical Oceanography, vol. 5 of Oceanography Series* (Elsevier, 1968).
9. M. G. Solonenko and C. D. Mobley, "Inherent optical properties of jerlov water types," Appl. Opt. **54**(17), 5392–5401 (2015).
10. H. Barth, K. Grisard, K. Holtsch, *et al.*, "Polychromatic transmissometer for in situ measurements of suspended particles and gelbstoff in water," Appl. Opt. **36**(30), 7919–7928 (1997).
11. G. Johnsen, M. Ludvigsen, A. Sørensen, *et al.*, "The use of underwater hyperspectral imaging deployed on remotely operated vehicles - methods and applications," IFAC-PapersOnLine **49**(23), 476–481 (2016).
12. B. Liu, Z. Liu, S. Men, *et al.*, "Underwater hyperspectral imaging technology and its applications for detecting and mapping the seafloor: A review," Sensors **20**(17), 4962 (2020).
13. D. M. Kocak, F. R. Dalgleish, F. M. Caimi, *et al.*, "A focus on recent developments and trends in underwater imaging," Mar. Technol. Soc. J. **42**(1), 52–67 (2008).
14. P. Risholm, J. Thorstensen, J. T. Thielemann, *et al.*, "Real-time super-resolved 3d in turbid water using a fast range-gated cmos camera," Appl. Opt. **57**(14), 3927–3937 (2018).
15. H. R. Gordon, "Equivalence of the point and beam spread functions of scattering media: a formal demonstration," Appl. Opt. **33**(6), 1120–1122 (1994).
16. O. V. Kopelevich and E. M. Mezhericher, *Calculation of spectral characteristics of light scattering by sea water* (Izv. Akad. Nauk SSSR, Fiz. Atmos. Okeana., 19(2), 144, 1983).
17. H. R. Gordon and A. Y. Morel, *Remote assessment of ocean color for interpretation of satellite visible imagery: A review, vol. 4 of Lecture notes on coastal and estuarine studies* (Springer, 1983).
18. W. H. Richardson, "Bayesian-based iterative method of image restoration*," J. Opt. Soc. Am. **62**(1), 55–59 (1972).
19. L. B. Lucy, "An iterative technique for the rectification of observed distributions," The Astronomical Journal **79**, 745 (1974).
20. K. J. Voss and B. J. Frew, "Aspects of the point spread function in the coastal zone," in *Ocean Optics XIII*, vol. 2963 S. G. Ackleson and R. J. Frouin, eds. (SPIE, 1997), pp. 566–569.
21. European Machine Vision Association, Emva standard 1288, standard for characterization of image sensors and cameras, release 3.1, (2016).
22. H. Grahn and P. Geladi, eds., *Techniques and applications of hyperspectral image analysis* (J. Wiley, 2007).
23. K. J. Voss and H. Zhang, "Bidirectional reflectance of dry and submerged labsphere spectralon plaque," Appl. Opt. **45**(30), 7924–7927 (2006).
24. S. Q. Duntley, "Underwater lighting by submerged lasers and incandescent sources," Scripps Institution of Oceanography (1971).
25. J. Petzold Theodore, *Volume Scattering Functions for Selected Ocean Waters* (UC San Diego: Scripps Institution of Oceanography, 1972).
26. A. Laux, R. Billmers, L. Mullen, *et al.*, "The a, b, c s of oceanographic lidar predictions: a significant step toward closing the loop between theory and experiment," J. Mod. Opt. **49**(3-4), 439–451 (2002).
27. A. Maccarone, A. McCarthy, X. Ren, *et al.*, "Underwater depth imaging using time-correlated single-photon counting," Opt. Express **23**(26), 33911–33926 (2015).
28. H. M. Oubei, C. Shen, A. Kammoun, *et al.*, "Light based underwater wireless communications," Jpn. J. Appl. Phys. **57**(8S2), 08PA06 (2018).
29. R. M. Pope and E. S. Fry, "Absorption spectrum (380–700 nm) of pure water. ii. integrating cavity measurements," Appl. Opt. **36**(33), 8710–8723 (1997).
30. D. Stramski, M. Babin, and S. B. Woźniak, "Variations in the optical properties of terrigenous mineral–rich particulate matter suspended in seawater," Limnol. Oceanogr. **52**(6), 2418–2433 (2007).
31. M. Jonasz and G. Fournier, *Light Scattering by Particles in Water: Theoretical and Experimental Foundations* (Elsevier, 2007).
32. R. A. Reynolds, D. Stramski, V. M. Wright, *et al.*, "Measurements and characterization of particle size distributions in coastal waters," J. Geophys. Res.: Oceans **115**(C8), 1 (2010).
33. S. Prahl, "miepython: Pure python implementation of mie scattering," (2023).
34. J. Wiscombe, "Mie Scattering Calculations: Advances in Technique and Fast, Vector-speed Computer Codes," (1979).
35. W. M. Haynes, *CRC Handbook of Chemistry and Physics*, vol. 91st ed., p. 4-139 (CRC Press Inc., 2011).
36. *Kirk-Othmer encyclopedia of chemical technology*, A John Wiley & Sons, Inc., publication (Wiley-Interscience, 2004), 5th ed.
37. K. J. Voss, "Simple empirical model of the oceanic point spread function," Appl. Opt. **30**(18), 2647–2651 (1991).
38. C. Mobley, *Light and water: Radiative transfer in natural waters* (Academic Press, 1994).
39. G. D. Boreman, *Modulation transfer function in optical and electro-optical systems, vol. Volume TT 121 of Tutorial texts in optical engineering* (SPIE Press, 2021), second edition ed.
40. E. Hecht, *Optik* (Oldenbourg, München and Wien, 1999), 2nd ed.
41. J. Watson and Z. Oliver, eds., *Subsea Optics and Imaging*, Woodhead Publishing Series in Electronic and Optical Materials (Woodhead Publishing, 2013).

Optics EXPRESS

42. X. Sun, M. Kong, O. Alkhazragi, *et al.*, "Non-line-of-sight methodology for high-speed wireless optical communication in highly turbid water," Opt. Commun. **461**, 125264 (2020).
43. A. Maccarone, K. Drummond, A. McCarthy, *et al.*, "Submerged single-photon lidar imaging sensor used for real-time 3d scene reconstruction in scattering underwater environments," Opt. Express **31**(10), 16690–16708 (2023).